Dalton Transactions

ROYAL SOCIETY OF CHEMISTRY

PAPER

View Article Online
View Journal

Cite this: DOI: 10.1039/d5dt02997j

Proton-conducting coordination polymers formed from bipyridine phosphonate ligands

Prajakta Mohan Ramteke,[a,b] Tomáš Plecháček, [c] Matouš Kloda, [a] Jan Rohlíček,[d] Anna Vykydalová,[a,e] Klára Melánová, [c] Dmytro Bavol,[a] Karel Škoch,[a] Marco Taddei, [f] Jan Demel [a] and Jan Hynek *[a]

Phosphonate-based linkers remain underexplored for constructing proton-conductive coordination polymers. We synthesized three new coordination polymers, ICR-25, ICR-26, and ICR-27, employing two new phosphonate ligands derived from 4,4′-bipyridine: 4,4′-bipyridine-2,2′,6,6′-tetraphosphonic acid (**H_8BipyTP**) and 4,4′-bipyridine-2,2′-diphosphonic acid (**H_4BipyDP**), with Ca^{2+} (ICR-25), Al^{3+} (ICR-26), and Mg^{2+} (ICR-27) ions. These materials represent new members of the limited family of N-heteroaromatic phosphonate frameworks. ICR-25 and ICR-26 contain hydrophilic voids with bound water molecules, while ICR-27 is a nonporous layered structure. In the structure of ICR-25, there are numerous acidic –OH groups, while ICR-26 is characterized by the presence of uncoordinated N heteroatoms. The proton conductivities of ICR-25 and ICR-26 are measured at relative humidity values of 75% and 92%, yielding the maximum value of 2.0×10^{-4} S cm^{-1}, which is achieved by ICR-26 at 92% humidity and a temperature of 306 K. Activation energies indicate the vehicle mechanism of proton transport in ICR-25 and the proton-hopping (Grotthuss) mechanism in the case of ICR-26. We thereby propose that using the N-heteroaromatic phosphonate ligands is an efficient method for the construction of proton-conducting coordination polymers.

Received 16th December 2025,
Accepted 5th March 2026

DOI: 10.1039/d5dt02997j

rsc.li/dalton

Introduction

Proton conductivity is one of the highly demanded properties of the currently developed materials, mainly due to their practical use as the key components of proton-exchange membrane fuel cells. Crystalline coordination polymers and, specifically, metal–organic frameworks (MOFs) are widely studied materials for proton conduction due to their ordered structure, enormous chemical and topological versatility and, in the case of MOFs, porous character.[1,2] The design of proton-conductive porous frameworks requires robustness of the system and the mobility of protons within the material. High crystallinity of the materials is needed to enable the visualization of the structure and elucidation of the proton conduction mechanism, while porous character is beneficial for the incorporation of additional carrier molecules, facilitating proton transport. For these reasons, MOFs, with their high crystallinity, porous character, and tunability of the size and chemical character of the pores, are promising candidates for proton-conducting materials.[3,4]

The significant amount of work that has been already done on proton-conducting MOFs draws upon three main strategies to enhance the proton conductivity properties,[5] which are the (i) tuning of pore size and topology to create an extensive H-bonded network;[6] (ii) introduction of hydrophilic functional groups, such as quaternary ammonium salts,[7] hydroxyls,[8] carboxylates,[9] sulfonates,[10–12] phosphonates[13] or phosphinates,[14] as proton sources; and (iii) incorporation of guest molecules, such as N-rich heterocycles (such as triazole,[15] imidazole,[16] and histamine[17]) and inorganic acids,[18] into the pores as proton transfer agents. It has been seen that the introduction of additional hydrophilic functional groups leads to the creation of an extended hydrogen-bonded network, promoting proton conductivity *via* the Grotthuss (or proton hopping) mechanism,[19] while in the case of MOFs containing hydrophilic guest molecules as proton carriers, the vehicle mechanism is more preferred.[20]

One of the main challenges of proton-conducting MOFs is their stability in elevated air humidity and temperature. The

[a]*Institute of Inorganic Chemistry of the Czech Academy of Sciences, Husinec-Řež 1001, 25068 Řež, Czech Republic. E-mail: hynek@iic.cas.cz*
[b]*Department of Inorganic Chemistry, Faculty of Science, Charles University, Hlavova 2030, 12840 Prague, Czech Republic*
[c]*Center of Materials and Nanotechnologies, Faculty of Chemical Technology, University of Pardubice, Studentská 95, 53210 Pardubice, Czech Republic*
[d]*Institute of Physics of the Czech Academy of Sciences, Na Slovance 1999/2, 18221 Praha, Czech Republic*
[e]*Polymer Institute, Slovak Academy of Sciences, Dúbravská Cesta 9, 84541 Bratislava, Slovakia*
[f]*Department of Chemistry and Industrial Chemistry, INSTM Research Unit, University of Pisa, Via G. Moruzzi 13, Pisa I-56124, Italy*

widely used MOFs based on carboxylate ligands often undergo gradual hydrolysis[21] or, even in the case of hydrolytically stable structures, suffer from structural degradation under the measurement conditions.[22] In contrast, ligands based on organophosphorus acids (phosphonic[23] (RPO_3H_2) or phosphinic[24] ($R^1R^2PO_2H$) acids) provide much more robust structures. Moreover, the phosphonate groups containing three oxygen atoms can remain partially protonated in the resulting frameworks and serve as a source of protons.[25] On the other hand, phosphonate and phosphinate ligands often tend to provide compact non-porous structures.[26,27] As the rational design and prediction of the resulting structures are complicated, the porous phosphonate frameworks represent only a small part of the known MOFs.[4] In spite of that, due to their excellent stability and possibilities of tuning the proton mobility, phosphonate MOFs are an important class of proton-conducting materials.[28] The usual strategy for the enhancement of proton conductivity is employing ligands with multiple phosphonate groups, a part of which can remain protonated and serve as proton sources.[29] Sometimes, the phosphonate functional groups are combined with another type of electron donors, *e.g.* nitrogen atoms originating from aromatic heterocycles.[30] When a suitable structure with hydrophilic pores and proton-donating groups is obtained, proton conductivity exceeding the value of 10^{-2} S cm^{-1} can be achieved at temperatures over 70 °C and relative humidity reaching almost 100%.[31–33]

In this paper, we describe the synthesis of two new ligands based on a 4,4′-bipyridine backbone, namely 4,4′-bipyridine-2,2′-diphosphonic acid (**H_4BipyDP**) and 4,4′-bipyridine-2,2′,6,6′-tetraphosphonic acid (**H_8BipyTP**), and their utilization for the construction of coordination polymers. From these ligands, three new materials are prepared: ICR-25, based on Ca^{2+} ions and the **H_8BipyTP** ligand, and ICR-26 and ICR-27, based on the **H_4BipyDP** ligand with Al^{3+} and Mg^{2+}, respectively (ICR = Institute of Inorganic Chemistry, Řež). The ligands combine heterocyclic nitrogen and phosphonate donor groups that can stay partially free and available for protonation in the resulting framework, thereby facilitating the proton conduction. To the best of our knowledge, we are reporting the first example of a ligand containing multiple phosphonate groups along with multiple N-heteroatomic donor groups.

Experimental section

Materials and instrumental methods

A list of the materials used and a description of the instrumental methods are given in the SI.

Synthesis of organic linkers

Descriptions of the synthetic procedures providing the organic linkers are given in the SI.

Preparation of ICR-25

A Teflon-lined stainless-steel autoclave (Berghof DAB-2) was charged with 22.0 mg (0.046 mmol) of **H_8BipyTP**, 44.0 mg of $Ca(NO_3)_2{\cdot}4H_2O$ (0.186 mmol), and 10 mL of water. The autoclave containing the reaction mixture was maintained at 100 °C under autogenous pressure for 72 h. After cooling, the resulting white solid was collected by centrifugation (Hettich Rotina 380 R, 11 000 rpm, 10 min), washed three times with water and three times with acetone, and air-dried.

Preparation of ICR-26

A Teflon-lined stainless-steel autoclave (Berghof DAB-2) was charged with 80.0 mg (0.25 mmol) of **H_4BipyDP**, 120.0 mg of $AlCl_3{\cdot}6H_2O$ (0.50 mmol), 500 mg of oxalic acid (5.5 mmol), and 10 mL of water. The autoclave containing the reaction mixture was maintained at 120 °C under autogenous pressure for 24 h. After cooling, the resulting white solid was collected by centrifugation (Hettich Rotina 380 R, 11 000 rpm, 10 min), washed three times with water and three times with acetone, and air-dried.

Preparation of ICR-27

A Teflon-lined stainless-steel autoclave (Berghof DAB-2) was charged with 80.0 mg (0.25 mmol) of **H_4BipyDP**, 128.0 mg of $MgNO_3{\cdot}6H_2O$ (0.50 mmol), and 10 mL of water. The autoclave containing the reaction mixture was maintained at 250 °C under autogenous pressure for 24 h. After cooling, the resulting white solid was collected by centrifugation (Hettich Rotina 380 R, 11 000 rpm, 10 min), washed three times with water and three times with acetone, and air-dried.

Adsorption measurement

The adsorption isotherms of argon at 87 K and CO_2 at 195 K were recorded using a 3P micro 300 instrument (3P Instruments) equipped with CryoTune units. Prior to the measurement, the samples were degassed for 16 h under a dynamic vacuum at the temperature that is specified individually for each experiment. The specific surface area was calculated using the Brunauer–Emmett–Teller (BET) analysis in the 0.005–0.1p/p_0 range. The adsorption of water vapour was measured using a Belsorp Max II instrument. The measurement was carried out at 298 K. Before the measurement, the ICR-25 sample was degassed at room temperature for 24 h, and the ICR-26 and ICR-27 samples were degassed at 120 °C for 24 hours under a dynamic vacuum.

Single crystal X-ray diffraction

Single crystal X-ray diffraction used for the determination of the structures of ICR-25 and ICR-27 was performed on a Rigaku XtaLAB Synergy S diffractometer equipped with a Cu (Cu Kα radiation; λ = 1.54184 Å) micro-focus X-ray source and a Hybrid Pixel Array Detector (HyPix-6000HE). The samples were kept at 100 K during the data collection using an Oxford Cryosystems (Cryostream 800) cooling device. CrysAlis Pro software was used for the data collection, cell refinement, data reduction, and absorption correction.[34] Data were corrected for absorption effects using empirical absorption correction (spherical harmonics), implemented in the SCALE3 ABSPACK scaling algorithm, and numerical absorption correction based

on Gaussian or analytical integration over a multifaceted crystal model. The structures were solved with the ShelXT[35] structure solution program using intrinsic phasing and refined with the ShelXL refinement package[36] using least squares minimisation as implemented in Olex2.[37] Anisotropic displacement parameters were refined for all non-H atoms. The hydrogen atoms were localized on a difference Fourier map or calculated in idealized positions.

Powder X-ray diffraction

The structure of ICR-26 was solved from the respective powder X-ray diffraction (XRD) pattern. The data were collected using the Debye–Scherrer transmission configuration on the PANalytical Empyrean powder diffractometer (Cu Kα radiation; λ = 1.54184 Å), which was equipped with a focusing mirror, capillary holder, and PIXCel[3D] detector. The sample was ground and placed in the 0.5 mm borosilicate-glass capillary. The crystal structure was solved using the SuperFlip program[38] and manual placement onto the Fourier maps in the MCE program.[39] The model was completed and refined in Jana2020[40] using bond-length and bond-angle restraints for the 4,4′-bipyridine and oxalic acid moieties, while the positions of other atoms in the structure were refined freely. Carbon, nitrogen, and oxygen atoms shared isotropic atomic displacement parameters, and phosphorus and aluminium were refined freely.

Proton conductivity measurements

Samples for the proton conductivity measurements were prepared by pressing powdered materials into round pellets with a thickness (L) of approximately 1 mm using a pressure of 92 MPa, to which 0.2 cm^2 Au-coated stainless-steel electrodes were mechanically pressed. The conductivity of the samples was measured with a Metrohm Autolab PGStat12 instrument in a frequency range from 0.1 Hz to 1 MHz with a signal amplitude of 200 mV. The impedance data in a complex impedance plot were analysed by an equivalent circuit approach using ZSimpWin software.[41] The chosen equivalent electrical circuit used for fitting consisted of a parallel arrangement of the resistance (R_1, R_2) and a constant phase element (CPE), as defined by Barsoukov and Macdonald.[42] The fit provides the value of resistance (R). For the calculation of proton conductivity (σ) of the samples, we used the relationship $\sigma = L/RA$, where A is area of the electrodes, and L stands for the distance between them.

Results and discussion

Synthesis

The presented MOFs are based on 4,4′-bipyridine di- and tetraphosphonate linkers (**H_4BipyDP** and **H_8BipyTP**, respectively), which have not been reported. The linkers were prepared by the oxidation of 4,4′-bipyridine to 4,4′-bipyridine-*N*,*N*′-dioxide (**1**),[43] followed by deoxygenative phosphorylation, as shown in Scheme 1. The resulting tetraethyl 4,4′-bipyridine-2,2′-diphosphonate (**2**) was hydrolysed to **H_4BipyDP**. The tetraphosphonate analogue, **H_8BipyTP**, was prepared by an analogous procedure using **2** as a starting material. The detailed procedure is described in the SI. This reaction path was previously described for pyridine, yielding 2-pyridinylphosphonic acid.[44] Interestingly, when it is applied to the 4,4′-bipyridine system,

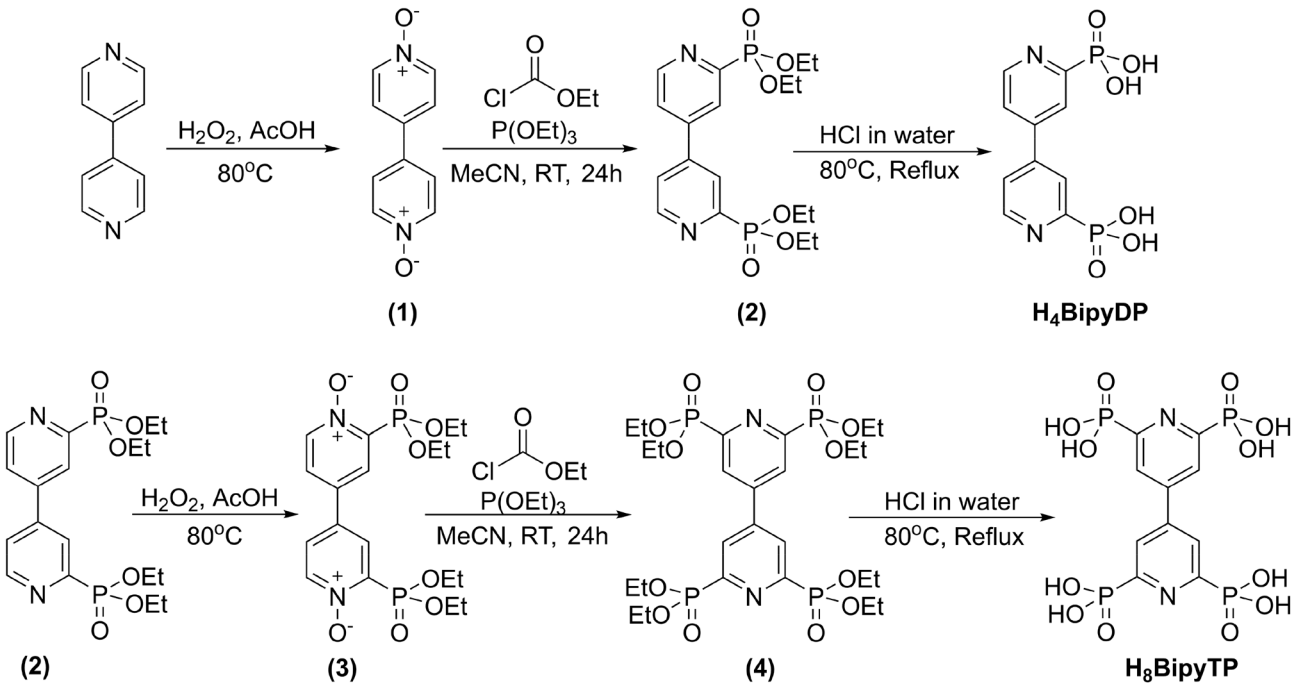

Scheme 1 Schematic of the synthesis of the **H_4BipyDP** and **H_8BipyTP** linkers.

it provides di- and tetra-phosphonate selectively in the first and second phosphorylation, respectively, without the occurrence of mono- or tri-substituted byproducts. This method represents a convenient and cost-effective path to obtain bipyridine-based phosphonate ligands, as compared to the more traditional methods involving coupling reactions, which require the usage of costly halogenated precursors, palladium catalysts and inert atmosphere.[45] The structure and purity of all prepared organic precursors were confirmed by ^{1}H, ^{13}C, and ^{31}P NMR spectroscopy (Fig. S1–S17) and high-resolution mass spectrometry (HRMS), and the crystal structure of the tetraethyl ester (**2**) was determined by SC-XRD (Fig. S18). Both linker molecules were also analysed by CHN combustion analysis. The content of the elements in **H_4BipyDP** was consistent with the calculated values. In the case of **H_8BipyTP**, the content of C and N was relatively low, and the content of H was higher than expected, which was caused by the presence of water due to the strong hygroscopicity of the compound. ICR-25 was prepared by the hydrothermal crystallization of the **H_8BipyTP** linker with $Ca(NO_3)_2{\cdot}4H_2O$ at 100 °C. ICR-26 and ICR-27 were prepared by the hydrothermal crystallization of the **H_4BipyDP** linker with $AlCl_3{\cdot}6H_2O$, along with oxalic acid and $MgNO_3{\cdot}6H_2O$, respectively. ICR-26 was obtained at 120 °C, while for the crystallization of ICR-27, a temperature of 250 °C had to be applied.

Structural determination

In the case of ICR-25 and ICR-27, the samples contained small crystals that allowed structural determination using single-crystal X-ray diffraction. On the other hand, ICR-26 could be obtained only in the form of microcrystalline powder; therefore, its structure was solved from the powder XRD data.

ICR-25 crystallized in the monoclinic $P2_1/n$ space group. The monoclinic angle was close to 90°; however, attempts to solve the structure in an orthorhombic space group did not yield satisfactory results (Table S1). The asymmetric unit contained eight ligands and nine Ca^{2+} ions, and the remaining positive charge was compensated by bridging oxygen species. The structure was composed of heptacoordinated Ca^{2+} ions interconnected *via* **BipyTP^{8-}** linkers containing two heteroaromatic nitrogen and four phosphonate donor groups (Fig. 1). Out of the nine Ca^{2+} ions in the asymmetric unit, eight were coordinated by one nitrogen and six oxygen atoms, out of which 4–5 originated from phosphonate groups and the remaining 1–2 from coordinated water molecules. The remaining Ca^{2+} ion was coordinated only by oxygen atoms belonging to phosphonate groups, water molecules, or bridging oxygen moieties. The phosphonate groups present in the structure adopted several coordination modes; the majority of phosphonate groups were bridging two Ca^{2+} cations either by two oxygen atoms (μ_2,η^2) or by a single oxygen (μ_2,η^1). Apart from that, the phosphonate groups bridging three Ca^{2+} cations using two oxygen atoms (μ_3,η^2) could be recognized (Fig. S19). The detailed view of the crystal structure showed that each asymmetric unit contained 64 phosphonate groups, out of which 32 were coordinated in μ_2,η^2, 28 in μ_2,η^1, and the remaining 4 in μ_3,η^2 coordination modes. The phosphonate groups present in the structure are most likely to occur in the monoprotonated form ($-PO_3H^-$); however, the precise determination of the protonation state from the XRD data was problematic due to the quality of the crystals and the delocalization of protons over the phosphonate groups. The polymeric structure of ICR-25 was composed of columns of stacked linkers oriented along the *x*-axis, which were interconnected by the Ca^{2+} nodes. The structure contained cylindrical voids with a diameter ranging from 2.5 to 4.5 Å (as calculated by the PoreBlazer software[46]), also oriented along the *x*-axis (Fig. S19). The pore walls were decorated with water molecules and oxygen atoms originating from the coordinated phosphonates. Although all of the heterocyclic nitrogen atoms were coordinated and thus not available for protonation, the structure contained numerous residual –OH groups on the phosphonate moieties, and therefore, it should be suitable for proton conduction.

For the preparation of ICR-26, a combination of **BipyDP^{4-}** and oxalate ligands was used. The use of oxalate co-ligand along with phosphonate linkers is a powerful and widely employed strategy to obtain well-crystalline frameworks;[47] however, to the best of our knowledge, we are reporting the first example of such a material based on Al^{3+} cations. The structure of ICR-26 (Fig. 2) consisted of Al^{3+} cations octahedrally coordinated by four oxygen atoms originating from the phosphonate groups of the **BipyDP^{4-}** linker and two other oxygen atoms belonging to the oxalate ligands. The oxalate ligands were coordinated by two oxygen atoms, both of which were linked to the same Al^{3+} cation, forming 5-membered chelate rings. All phosphonate groups were fully deprotonated and coordinated by all three oxygen atoms to three different Al^{3+} ions, adopting a μ_3,η^3 coordination mode. Therefore, in contrast with that of ICR-25, the structure of ICR-26 did not provide any cleavable –OH groups, which could serve as sources of protons. On the other hand, unlike other examples of aluminium coordination polymers based on N-heterocyclic linkers,[48] none of the nitrogen atoms from the 4,4′-bipyridine moieties was involved in Al^{3+} coordination, which made them available for facilitating proton transport by serving as a proton acceptor (Fig. S21). The structure of ICR-26 contained only small cavities with a diameter of 0.7–1.5 Å oriented along the *z* axis (Fig. S22). The oxygen atoms of the water molecules inside the small cavity in the structure were visible in the difference Fourier map, exhibiting disorder over two sites with refined site occupancy, suggesting 50% probability at each position. The final Rietveld plot showed good agreement between the measured data and the refined model (Fig. 2).

The structure of ICR-27 (Fig. 3) was composed of parallel infinite chains of octahedrally coordinated Mg^{2+} cations oriented along the *y* axis, which were interconnected by the 4,4′-bipyridine spacers oriented perpendicularly to the chains (Fig. S23). The Mg^{2+} cations were connected by the O–P–O bridges from the phosphonate groups of the linker molecules. Each Mg^{2+} was coordinated by four oxygen atoms originating

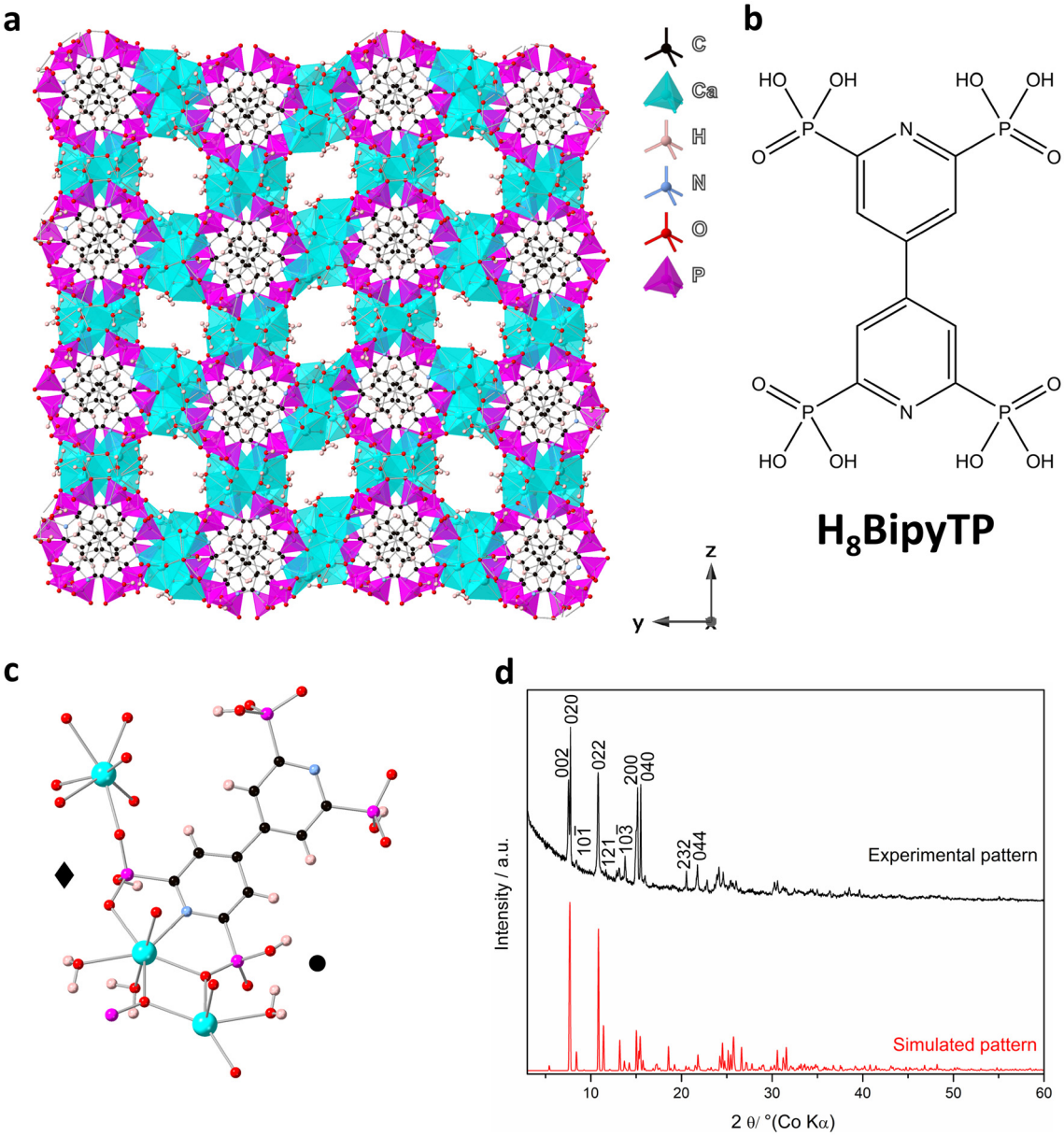

Fig. 1 (a) Crystal structure of ICR-25 in the (100) projection, showing the characteristic 1D channels. (b) Structural formula of the **H_8BipyTP** ligand. (c) Detail of the coordination of the **H_8BipyTP** ligand in the ICR-25 structure, showing the two most frequent coordination modes of the $-PO_3H^-$ groups: μ_2,η^2 (◆) and μ_2,η^1 (●). (d) Comparison of the experimental powder XRD pattern with the pattern simulated from the obtained crystal structure.

from the phosphonate groups of the **$BipyDP^{4-}$** linker, one water molecule, and an aromatic nitrogen of the 4,4′-bipyridine body. All phosphonate groups in the structure were fully deprotonated, and all of the oxygen atoms were involved in the coordination of four different Mg^{2+} cations in total; therefore, the coordination mode could be denoted as μ_4,η^3. Since there were neither –OH groups nor uncoordinated nitrogen atoms of the aromatic rings in the structure of ICR-27, and it formed a non-porous compact structure, the material was unfortunately not suitable for proton conductivity; therefore, the respective studies on this material were omitted.

Characterization of the materials

The experimental powder XRD patterns of ICR-25 and ICR-27 (Fig. 1 and 3) were in good agreement with the respective simulated profiles generated from the obtained crystal structures, which demonstrated the reproducibility of the syntheses and phase purity of the samples. The results of CHN combustion analysis (Table S2) for ICR-25 and ICR-27 were in agreement with the empirical formulas obtained from the crystal structures. ICR-26 demonstrated lower-than-expected carbon content and higher-than-expected hydrogen content, which

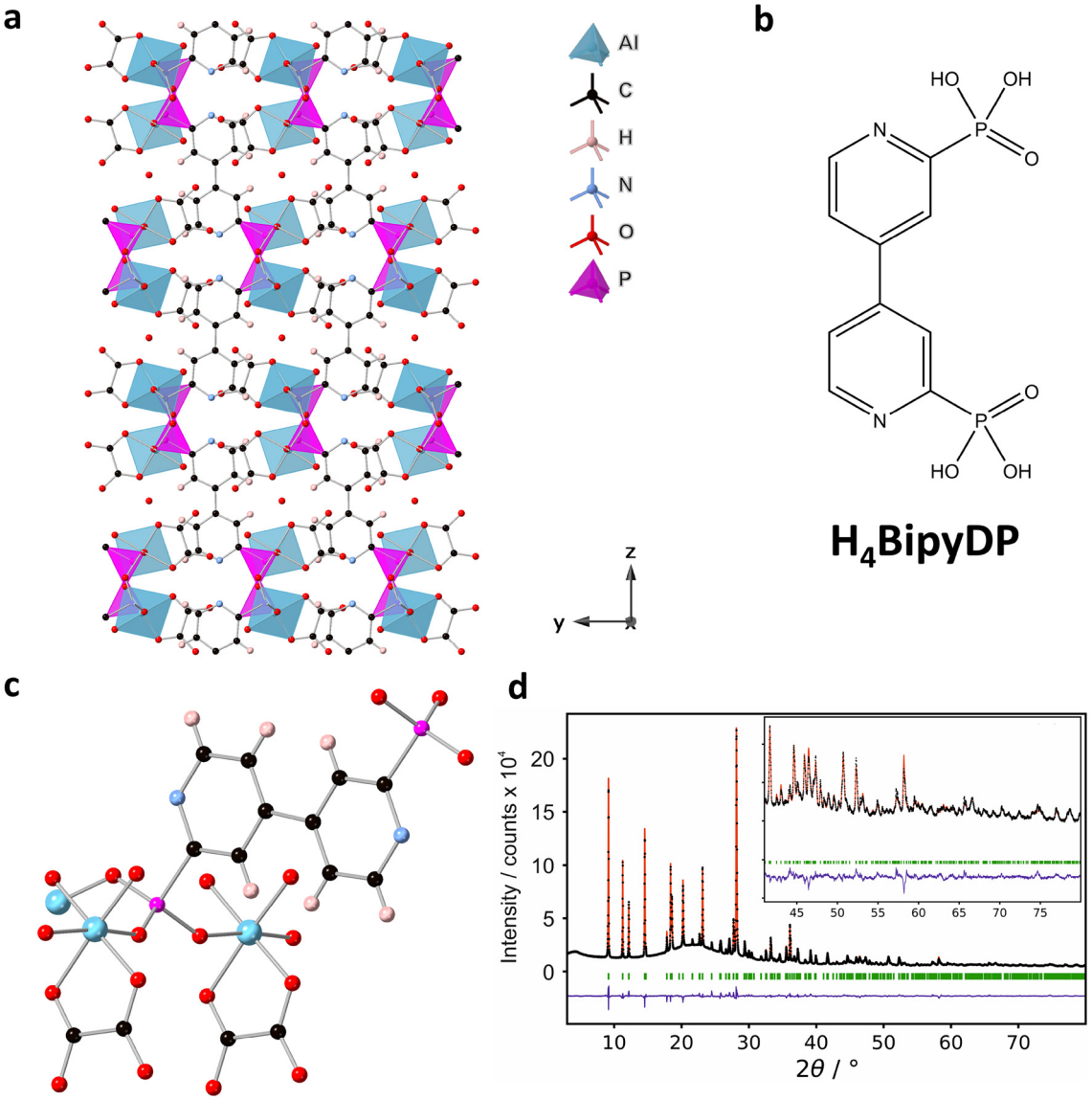

Fig. 2 (a) Crystal structure of ICR-26 in the (100) projection. (b) Structural formula of the **H_4BipyDP** ligand. (c) Detail of the coordination of the **H_4BipyDP** ligand in the ICR-26 structure, showing the phosphonate group in the μ_3,η^3 coordination mode and the oxalate anions, forming 5-membered chelate rings. (d) Final plot of the Rietveld refinement, where red line: calculated profile, black dots: measured data, blue line: difference curve, and green bars: Bragg's positions.

were probably caused by the hydration of the sample combined with the presence of partially uncoordinated phosphonates on the surface of crystallites.

The FTIR spectrum of ICR-25 (Fig. S24) showed a characteristic signal of O–H stretching vibration at 3296 cm^{-1}, which was significantly broadened, suggesting the presence of bigger clusters of water molecules and –OH groups, forming a hydrogen-bonded network inside the 1D channels of the material. In contrast, in the spectra of ICR-26 and ICR-27 (Fig. S25), the respective bands were narrow, demonstrating that the water molecules were isolated and did not form strong hydrogen bonds. The spectra of phosphonic acids contained several characteristic bands originating from the phosphonate groups; P═O stretching, P–O symmetric stretching, and P–O antisymmetric stretching vibrations, which were located at 1176, 1043, and 928 cm^{-1} and 1161, 1035, and 940 cm^{-1} in the case of **H_4BipyDP** and **H_8BipyTP**, respectively. By deprotonation, the oxygen atoms of the phosphonate groups became equivalent, thereby reducing the number of P–O stretching bands to only two.[49] These bands could be observed in the spectra of ICR-26 and ICR-27, with fully deprotonated and η^3-coordinated phosphonate groups at 1154 and 1050 cm^{-1} or 1132 and 1003 cm^{-1}, respectively. A different situation arose in the case of ICR-25, with 4 different stretching bands that could be attributed to phosphonate groups at 1178, 1123, 1063, and 980 cm^{-1}, which pointed out partial protonation and the pres-

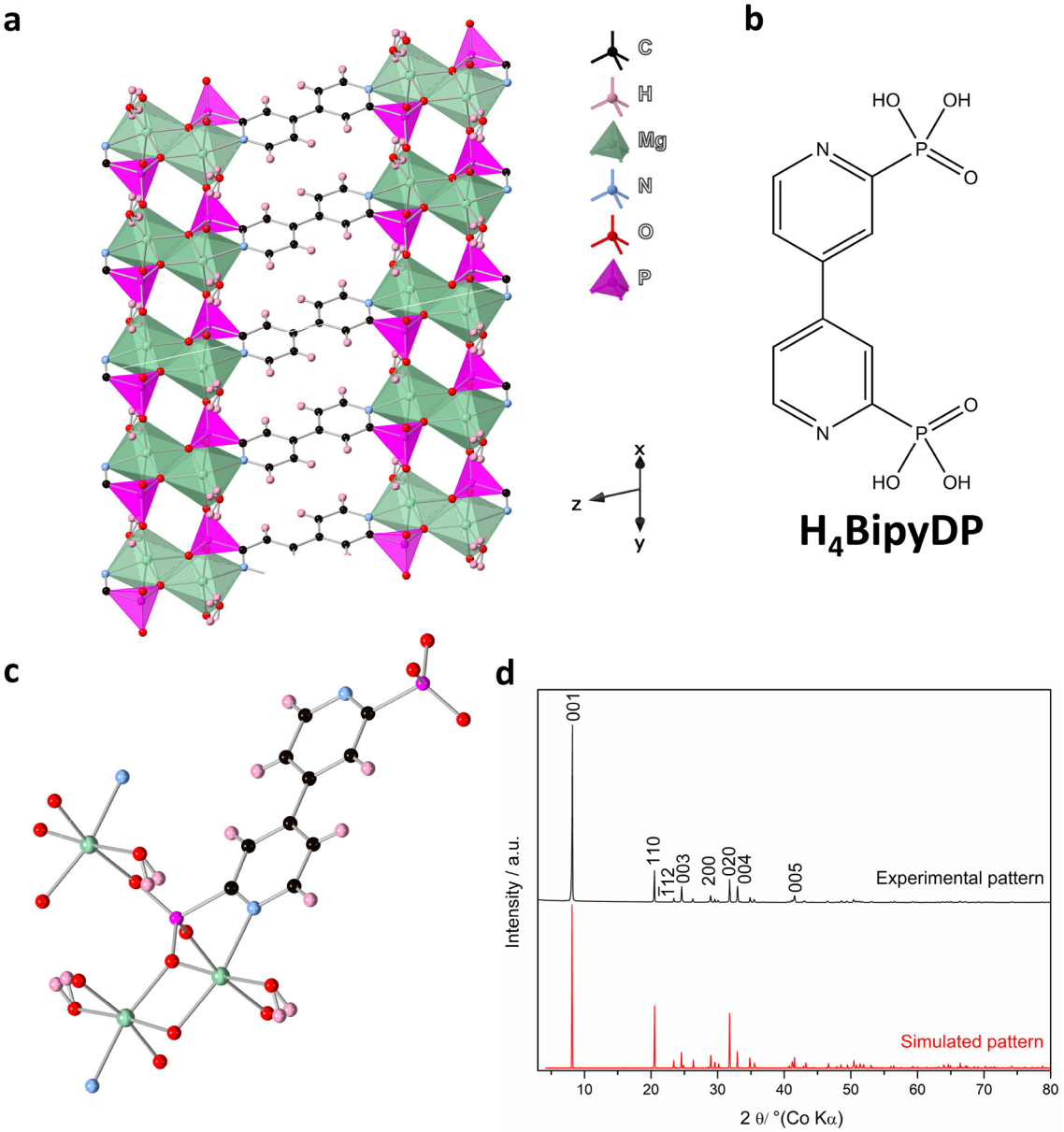

Fig. 3 (a) Crystal structure of ICR-27 in the (110) projection. (b) Structural formula of the **H_4BipyDP** ligand. (c) Detail of the coordination of the **H_4BipyDP** ligand in the ICR-27 structure, showing the phosphonate group in the μ_4,η^3 coordination mode and the coordinated H_2O molecules. (d) Comparison of the experimental powder XRD pattern with the pattern simulated from the obtained crystal structure.

ence of multiple coordination modes of the phosphonate groups in the structure. The presence of the oxalate ligands in the structure of ICR-26 could be elucidated by the appearance of sharp signals of C═O and C–O stretching vibrations at 1689 and 1431 cm^{-1}, respectively.

Thermogravimetric analyses showed significant differences among the individual materials. ICR-25 (Fig. S26) exhibited a significant weight loss of approximately 12 wt% already between 40 °C and 140 °C, with the maximum around 80 °C, accompanied by the release of water as detected by mass spectrometry (*m*/*z* 17 and 18). The differential scanning calorimetry (DSC) measurement (Fig. S27) revealed that the process was endothermic, with an enthalpy of 355 J g^{-1}, and irreversible. Therefore, we assumed that it corresponded to the loss of water molecules contained inside the channels, which were obviously strongly hydrated. In contrast, for ICR-26 (Fig. S27) and ICR-27 (Fig. S29), weight losses of only ~3 wt% and 0.1 wt%, respectively, were observed in this temperature region, pointing out a relatively low level of hydration of ICR-26 and the absence of adsorbed water in ICR-27. The later evolution of water from ICR-27 between 175 °C and 207 °C corresponded to the release of water molecules coordinated to the Mg^{2+} cations, and the observed weight loss (~8.8%) agreed with their theoretical content (9.1%). The combustion of the

organic linkers started at 534 °C for ICR-26, 565 °C for ICR-27, and 666 °C for ICR-25, which appeared to be the most thermally stable of the series. In the case of ICR-26, a significant weight loss accompanied by the evolution of CO_2 was observed already at temperatures between 285 °C and 360 °C. This obviously corresponded to the release of oxalate moieties from the structure, as it fitted the temperature range where aluminium oxalates usually decompose,[50] and the observed weight loss during the first main step of degradation (~30.0%) roughly corresponded to the calculated mass content of the oxalate moieties in the structure (25.5%). Interestingly, the linker combustion in ICR-27 proceeded in two steps; the first part of CO_2 evolved between 550 °C and 750 °C, and another portion seemed to be released above 900 °C.

As the crystal structures suggested the porous character of ICR-25 and ICR-26, the adsorption isotherms of Ar (87 K) were measured on the respective samples. However, the adsorption isotherms for ICR-25 (Fig. S30), which should contain micropores of 2.5–4.5 Å, did not reveal any porous character for either Ar or CO_2. The powder XRD pattern of ICR-25 recorded after the adsorption measurements (Fig. S31) showed a completely different diffraction pattern than at the beginning, suggesting the instability of the structure upon simultaneous heating and evacuation. On the other hand, when the material was activated only at RT, no porosity was detected either by Ar or by CO_2 adsorption. As all the performed characterization methods suggested, the hydrophilic channels of ICR-25 were filled with guest water molecules, which apparently could not be released under mild conditions, while elevated temperature led to the recrystallization of the material into a more preferable non-porous phase. In the case of ICR-26, the crystal structure suggested the presence of narrow micropores of 0.7–1.5 Å diameter, which was smaller than the kinetic diameter of Ar (3.40 Å), making adsorption into the pores impossible. Expectedly, the Ar and CO_2 adsorption measurements did not reveal the presence of micropores (Fig. S32). The structure of ICR-26 suggested the presence of water molecules; however, their removal did not open up the pores sufficiently for Ar or CO_2 adsorption. The powder XRD pattern of ICR-26 recorded after the adsorption measurements confirmed its stability under the conditions of activation (Fig. S33). The expected non-porous character of ICR-27 was confirmed experimentally by the measurement of the CO_2 adsorption isotherm, which did not demonstrate the presence of any pores (Fig. S34). The adsorption of water vapours, which is a key parameter affecting the usability of materials for proton conduction, was measured for ICR-25 and ICR-26. Although the materials did not reveal any porosity when examined by Ar adsorption, they demonstrated a significant adsorption of water. ICR-25, which was activated only at RT to avoid structural changes observed at high temperatures, reached water uptake of 365 $cm^3\ g^{-1}$ at p/p_0 = 0.99 (Fig. S35), which corresponded to the presence of 10 water molecules per one linker moiety and demonstrated the hydrophilic character of the material. ICR-26 displayed water uptake of 113 $cm^3\ g^{-1}$ at p/p_0 = 0.99 (Fig. S36), corresponding to the presence of 3 water molecules per one linker moiety, which was in agreement with the total content of water molecules suggested by the crystal structure. The mass loss upon activation was ~9%, which also corresponded to approximately 3 water molecules per one linker and further supported the hypothesis that the material could be fully dehydrated by vacuum heating, including the removal of coordinated water molecules, and then hydrated again by exposure to almost 100% relative humidity.

In order to get more information about the phase transformation that occurred in ICR-25 upon heating and evacuation, further experiments were performed. The variable temperature powder XRD patterns (Fig. S37) suggested that the phase transition was a multi-step process. First, the crystallinity of ICR-25 started to decrease, which could be observed at temperatures as low as 45 °C, continuing until around 80 °C, when the diffraction lines of the original phase almost disappeared. Upon further heating, a new crystalline phase was formed, as evidenced by a gradual increase in the intensity of the newly emerging reflections. The phase transition seemed to be an irreversible process, as the treated sample did not adopt the original XRD pattern after cooling (Fig. S38). As mentioned above, this finding was also supported by the DSC measurement (Fig. S27), where a cycle of heating–cooling–heating was performed, and during the cooling and repeated heating, no signs of a phase change were observed anymore. However, the original structure could be partially restored by water treatment in an autoclave at 100 °C for 72 h.

Proton conductivity

Two of the presented materials that contained potential voids occupied by water molecules and free functional groups, which could further facilitate the proton mobility, ICR-25 and ICR-26, were tested for proton conductivity. The measurements were performed at the relative humidity (RH) of 75% and 92% and in the temperature range of 295–337 K. The measurement temperature was intentionally kept below the temperature of the phase transition observed for ICR-25. In the case of ICR-25 at the RH of 75%, the obtained Nyquist plot (Fig. 4) was composed of two semicircles and was fitted by ($C(R(Q(RW))))$ equivalent circuit (Fig. S39). From the fit, two values of proton conductivity were obtained; one of them probably corresponded to the conductivity of the sample, while the second one could be attributed to conduction at grain boundaries. At RH of 92%, the second semicircle was visible only before the equilibrium state was achieved; during the equilibration, it gradually merged with the first one. The corresponding Nyquist plots were fitted by a ($Q(RW)$) equivalent circuit. The Nyquist plots obtained for ICR-26 corresponded to a single semicircle; therefore, they were fitted by ((QR)Q) equivalent circuit, from which the proton conductivity values were calculated.

The proton conductivity of ICR-25 (Table S3) reached values of up to 4.6×10^{-6} S cm^{-1}, which was achieved at RH of 75% and 335 K and made the material a moderate proton conductor among coordination polymers, such as the recently published material, BAM-5 (6.6×10^{-6} S cm^{-1} at 353 K and RH of 98%), which analogously combines a partially protonated

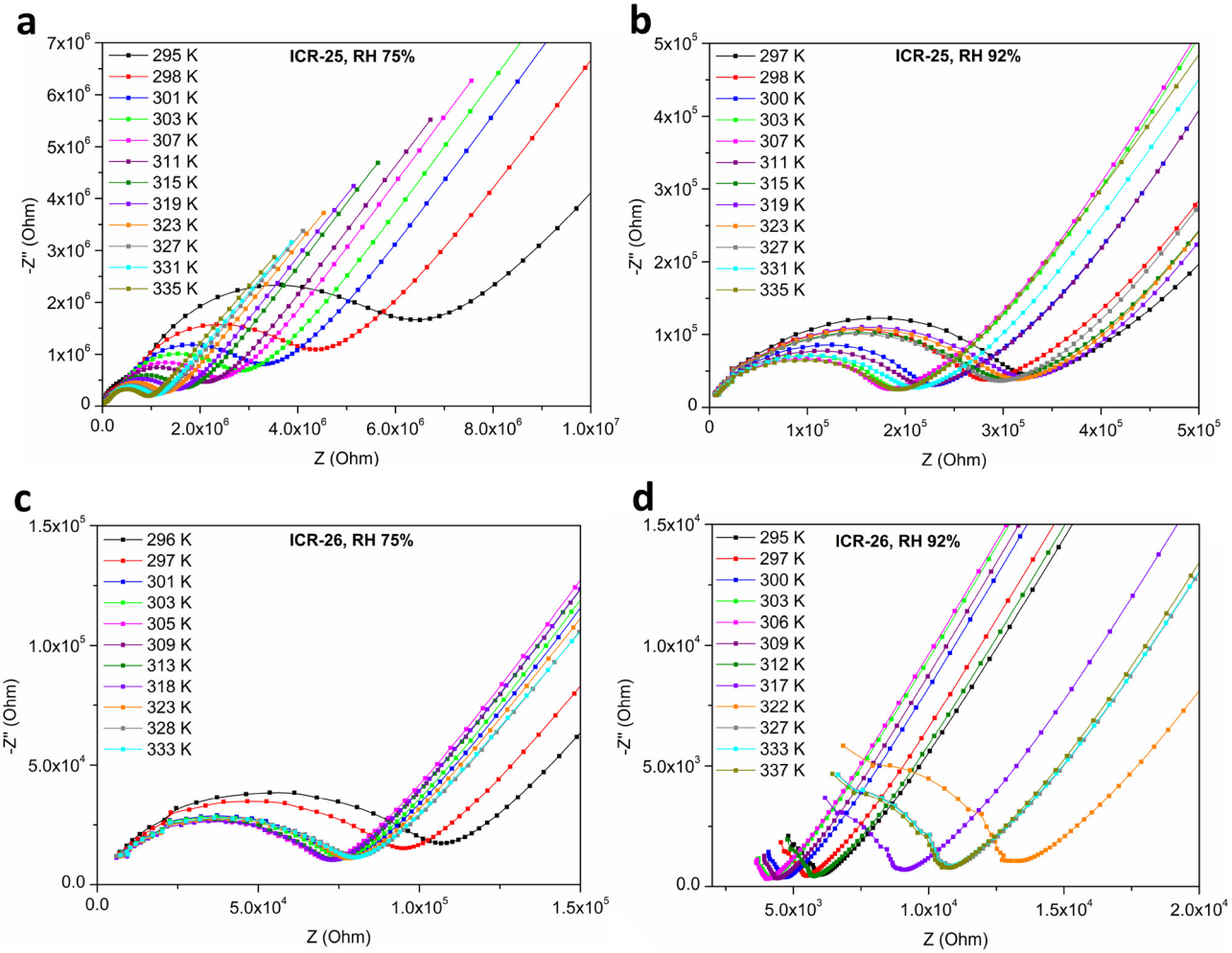

Fig. 4 Nyquist plots for ICR-25 measured at (a) 75% and (b) 92% relative humidity and for ICR-26 measured at (c) 75% and (d) 92% relative humidity. The measurements were performed at variable temperatures to observe the temperature dependence of the proton conductivity.

phosphonate linker with fully coordinated 4,4′-bipyridine co-ligands.[51] However, increasing RH to 92% did not bring any significant improvement of the proton conductivity performance. The powder XRD patterns of ICR-25 (Fig. S40) revealed that the material retained the original structure upon measurement, although the crystallinity decreased. The proton conductivity performance of ICR-26 was better than that of ICR-25 by almost two orders of magnitude, reaching the conductivity of up to 2.0×10^{-4} S cm^{-1}, which was achieved at RH of 92% and 303 K. This material revealed a similar performance to analogous coordination polymers based on a phosphonate linker and an N-heteroaromatic co-ligand, with partially uncoordinated N-atoms available for protonation, *e.g.* the values slightly exceeded the values for the $[Dy(H\text{-}HEDP)_2]\cdot H_3\text{-}TPI\cdot 4H_2O$ complex (6.2×10^{-5} S cm^{-1} at 303 K and RH of 100%) containing hydroxyethylidene diphosphonate (HEDP) and 2,4,5-tris(4-pyridyl)-imidazole (TPI).[52] In contrast with ICR-25, the increase in RH from 75% to 92% led to the improvement of the proton conductivity by more than one order of magnitude. The powder XRD patterns of ICR-26 after the proton conductivity measurements (Fig. S41) did not exhibit any changes, demonstrating the stability of the material under the applied measurement conditions.

The measured samples revealed an increasing trend in the conductivity only in a relatively narrow temperature window up to 305 K, except for ICR-25 at the relative humidity of 75%, where the conductivity increased throughout the entire studied temperature range. The phenomenon of decreasing proton conductivity above a specific temperature was attributed to the loss of proton carriers and could be encountered in a number of MOFs and coordination polymers.[53,54] For that reason, the activation energy of proton conduction was estimated only from the regions where the conductivity increased with temperature. The slopes of the respective Arrhenius plots (Fig. 5) provided activation energies of 0.40–0.53 eV for ICR-25 and 0.32–0.36 eV for ICR-26. These values suggested the vehicle mechanism of the proton transport in the case of ICR-25 and the Grotthuss mechanism for ICR-26. The proton conduction in ICR-25 seemed to be facilitated by water molecules contained inside the 1D channels, while in ICR-26, the

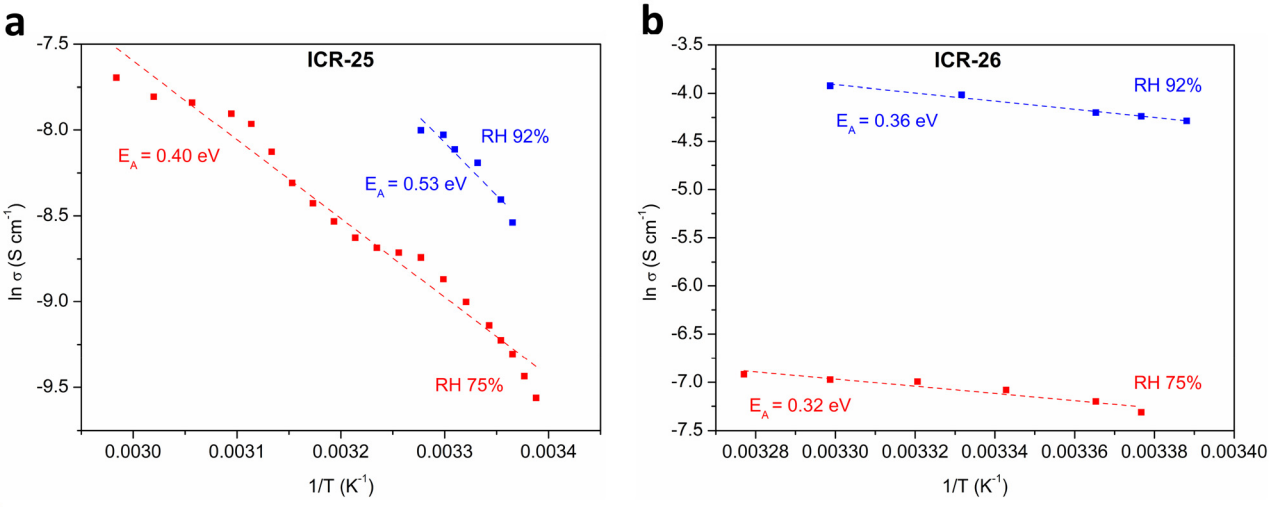

Fig. 5 Arrhenius plots for ICR-25 (a) and ICR-26 (b) at different humidities. The fit error is below 3%.

hopping of protons among the adsorbed water molecules and heteroaromatic nitrogen sites was likely to occur. In the case of ICR-25, the Arrhenius plots exhibited a significant deviation from linearity, which was probably caused by the complicated dynamic character of the structure containing different kinds of proton carriers, mainly protonated –OH groups, as well as both coordinated and uncoordinated water molecules, making the proton conduction a rather complex process with multiple contributions.

In general, the introduction of free heterocyclic N atoms, as well as free –OH groups, originating from partially protonated phosphonate groups, seems to be a suitable strategy for the preparation of proton-conducting phosphonate frameworks. The lower proton conductivity of ICR-25 compared with that of ICR-26 might be caused by the presence of too many uncoordinated phosphonate groups. Materials containing excessive free phosphonates have been described to restrict the motion of guest proton-carrier molecules by strong hydrogen bonding, thereby suppressing the proton conductivity.[55]

Conclusions

The di- and tetra-phosphonate ligands based on a 4,4′-bipyridine body, **H_4BipyDP** and **H_8BipyTP**, respectively, provided robust coordination polymers with various metals, namely ICR-25, ICR-26, and ICR-27. The structures of ICR-25 and ICR-26 contained potential voids occupied by guest water molecules and numerous free functional groups, either protonated, partially uncoordinated phosphonate groups or uncoordinated heteroaromatic nitrogen atoms from the bipyridine moieties, which appeared to facilitate proton movement. The proton conductivity of ICR-26 reached values of up to 2.0×10^{-4} S cm^{-1} at 92% relative humidity and 306 K, which made ICR-26 a moderate proton conductor among phosphonate coordination polymers, not reaching the performance of the best ones (10^{-2} S cm^{-1}),[31,56,57] but exceeding those of the majority of materials described in literature, displaying conductivity of 10^{-6}–10^{-5} S cm^{-1}.[23] In terms of proton conductivity, the presence of uncoordinated N atoms seemed to be more beneficial than partially protonated phosphonate groups. Employing phosphonate ligands based on N-heteroaromatic bodies can provide stable and easy-to-prepare coordination polymers, and we hope that this direction is worth further investigation.

Author contributions

P. M. R. – investigation and writing – original draft; T. P. – investigation and formal analysis; M. K. – investigation and formal analysis; J. R. – investigation and formal analysis; A. V. – investigation and formal analysis; K. M. – investigation; D. B. – investigation; K. S. – conceptualization; M. T. – validation; J. D. – supervision; and J. H. – project administration, resources, visualization, and writing – review & editing.

Conflicts of interest

There are no conflicts to declare.

Data availability

All the raw experimental data are deposited in the depository of the institution of the corresponding author and will be available upon the reader's request.

Supplementary information (SI) is available. See DOI: https://doi.org/10.1039/d5dt02997j.

CCDC 2499442, 2499447, 2499450 and 2503831 contain the supplementary crystallographic data for this paper.[58a–d]

Acknowledgements

The authors acknowledge the financial support from the Czech Science Foundation (no. 23-06562S). The maintenance of the PXRD and FTIR facilities was supported by Research Infrastructure NanoEnviCz, supported by the Ministry of Education, Youth and Sports of the Czech Republic under project no. LM2018124; the Ministry of Education, Youth and Sports of the Czech Republic and the European Union – European Structural and Investment Funds within the project Pro-NanoEnviCz II (project no. CZ.02.1.01/0.0/0.0/18_046/0015586). The authors thank Petr Bezdička, Jitka Bezdičková and Pavla Kurhajcová for the PXRD and TGA measurements.

References

1 G. K. Shimizu, J. M. Taylor and S. Kim, Proton conduction with metal–organic frameworks, *Science*, 2013, **341**, 354–355.
2 H. Furukawa, K. E. Cordova, M. O'Keeffe and O. M. Yaghi, The chemistry and applications of metal–organic frameworks, *Science*, 2013, **341**, 1230444.
3 P. Ramaswamy, N. E. Wong and G. K. Shimizu, MOFs as proton conductors – challenges and opportunities, *Chem. Soc. Rev.*, 2014, **43**, 5913–5932.
4 T. Zheng, W. Tan and L. M. Zheng, Porous metal phosphonate frameworks: construction and physical properties, *Acc. Chem. Res.*, 2024, **57**, 2973–2984.
5 M. Sadakiyo, T. Yamada and H. Kitagawa, Rational designs for highly proton-conductive metal–organic frameworks, *J. Am. Chem. Soc.*, 2009, **131**, 9906–9907.
6 M. Sadakiyo, T. Yamada, K. Honda, H. Matsui and H. Kitagawa, Control of crystalline proton-conducting pathways by water-induced transformations of hydrogen-bonding networks in a metal–organic framework, *J. Am. Chem. Soc.*, 2014, **136**, 7701–7707.
7 M. Sadakiyo, H. Ōkawa, A. Shigematsu, M. Ohba, T. Yamada and H. Kitagawa, Promotion of low-humidity proton conduction by controlling hydrophilicity in layered metal–organic frameworks, *J. Am. Chem. Soc.*, 2012, **134**, 5472–5475.
8 S. Biwas, J. Chakraborty, V. S. Parmar, S. P. Bera, N. Ganguli and S. Konar, Channel-assisted proton conduction behavior in hydroxyl-rich lanthanide-based magnetic metal–organic frameworks, *Inorg. Chem.*, 2017, **56**, 4956–4965.
9 A. Shigematsu, T. Yamada and H. Kitagawa, Wide control of proton conductivity in porous coordination polymers, *J. Am. Chem. Soc.*, 2011, **133**, 2034–2036.
10 W. J. Phang, H. Jo, W. R. Lee, J. H. Song, K. Yoo, B. Kim and C. S. Hong, Superprotonic conductivity of a UiO-66 framework functionalized with sulfonic acid groups by facile postsynthetic oxidation, *Angew. Chem., Int. Ed.*, 2015, **54**, 5142–5146.
11 F. Yang, G. Xu, Y. Dou, B. Wang, H. Zhang, H. Wu, W. Zhou, J. R. Li and B. Chen, A flexible metal–organic framework with a high density of sulfonic acid sites for proton conduction, *Nat. Energy*, 2017, **2**, 877–883.
12 D. K. Maity, K. Otake, S. Ghosh, H. Kitagawa and D. Ghoshal, Sulfonic group functionalized mixed ligand coordination polymers: synthesis, characterization, water sorption, and proton conduction studies, *Inorg. Chem.*, 2017, **56**, 1581–1590.
13 J. M. Taylor, K. W. Dawson and G. K. Shimizu, A water-stable metal–organic framework with highly acidic pores for proton-conducting applications, *J. Am. Chem. Soc.*, 2013, **135**, 1193–1196.
14 M. Kloda, T. Plecháček, S. Ondrušová, P. Brázda, P. Chalupský, J. Rohlíček, J. Demel and J. Hynek, Phosphinate MOFs formed from tetratopic ligands as proton-conductive materials, *Inorg. Chem.*, 2022, **61**, 7506–7512.
15 J. A. Hurd, R. Vaidhyanathan, V. Thangadurai, C. I. Ratcliffe, I. L. Moudrakovski and G. K. Shimizu, Anhydrous proton conduction at 150 °C in a crystalline metal–organic framework, *Nat. Chem.*, 2009, **1**, 705–710.
16 F.-M. Zhang, L.-Z. Dong, J.-S. Qin, W. Guan, J. Liu, S.-L. Li, M. Lu, Y.-Q. Lan, Z.-M. Su and H.-C. Zhou, Effect of imidazole arrangements on proton conductivity in metal–organic frameworks, *J. Am. Chem. Soc.*, 2017, **137**, 6183–6189.
17 D. Umeyama, S. Horike, M. Inukai, Y. Hijikata and S. Kitagawa, Confinement of mobile histamine in coordination nanochannels for fast proton transfer, *Angew. Chem., Int. Ed.*, 2011, **50**, 11706–11709.
18 X.-M. Li, L.-Z. Dong, S.-L. Li, G. Xu, J. Liu, F.-M. Zhang, L.-S. Lu and Y.-Q. Lan, Synergistic conductivity effect in a proton sources-coupled metal–organic framework, *ACS Energy Lett.*, 2017, **2**, 2313–2318.
19 D. A. Levenson, J. Zhang, P. M. Szell, D. L. Bryce, B. S. Gelfand, R. P. Huynh, N. D. Fylstra and G. K. Shimizu, Effects of secondary anions on proton conduction in a flexible cationic phosphonate metal–organic framework, *Chem. Mater.*, 2019, **32**, 679–687.
20 K.-D. Kreuer, A. Rabenau and W. Weppner, Vehicle mechanism, a new model for the interpretation of the conductivity of fast proton conductors, *Angew. Chem., Int. Ed. Engl.*, 1982, **21**, 208–209.
21 D. Bůžek, J. Hynek, M. Kloda, V. Zlámalová, P. Bezdička, S. Adamec and J. Demel, Zirconium-based metal–organic frameworks: the relation between linker connectivity, structure stability, and catalytic activity towards organophosphates, *Inorg. Chem. Front.*, 2024, **11**, 5319–5335.
22 J. Hynek, M. Kloda, M. Litecká, A. Vykydalová, J. Tolasz, M. Pospíšil, Z. Morávková, M. K. Chahal, L. Beneš, T. Plecháček and K. Melánová, Effect of elevated air humidity on the structure and proton conductivity of porphyrin-based Zr(IV)–MOFs, *Inorg. Chem.*, 2025, **64**, 15993–16004.
23 S.-S. Bao, G. K. H. Shimizu and L.-M. Zheng, Proton conductive metal phosphonate frameworks, *Coord. Chem. Rev.*, 2019, **378**, 577–594.
24 J. Hynek, P. Brázda, J. Rohlíček, M. G. S. Londesborough and J. Demel, Phosphinic acid based linkers: building

blocks in metal–organic framework chemistry, *Angew. Chem., Int. Ed.*, 2018, **57**, 5016–5019.
25 D. A. Levenson, J. Zhang, B. S. Gelfand, S. P. Kammampata, V. Thangadurai and G. K. Shimizu, Particle size dependence of proton conduction in a cationic lanthanum phosphonate MOF, *Dalton Trans.*, 2020, **49**, 4022–4029.
26 K. J. Gagnon, H. P. Perry and A. Clearfield, Conventional and unconventional metal–organic frameworks based on phosphonate ligands: MOFs and UMOFs, *Chem. Rev.*, 2012, **112**, 1034–1054.
27 J. Rohlíček, D. Bůžek, P. Brázda, L. Kobera, J. Hynek, J. Brus, K. Lang and J. Demel, Novel cerium bisphosphinate coordination polymer and unconventional metal–organic framework, *Crystals*, 2019, **9**, 303.
28 Y. Ye, L. Gong, S. Xiang, Z. Zhang and B. Chen, Metal–organic frameworks as a versatile platform for proton conductors, *Adv. Mater.*, 2020, **32**, 1907090.
29 Y. Enakieva, A. A. Sinelshchikova, M. S. Grigoriev, V. V. Chernyshev, K. A. Kovalenko, I. A. Stenina, A. B. Yaroslavtsev, Y. G. Gorbunova and A. Y. Tsivadze, Porphyrinylphosphonate-based metal–organic framework: tuning proton conductivity by ligand design, *Chem. – Eur. J.*, 2021, **27**, 1598–1602.
30 S. Begum, Z. Wang, A. Donnadio, F. Costantino, M. Casciola, R. Valiullin, C. Chmelik, M. Bertmer, J. Kärger, J. Haase and H. Krautscheid, Water-mediated proton conduction in a robust triazolyl phosphonate metal–organic framework with hydrophilic nanochannels, *Chem. – Eur. J.*, 2014, **20**, 8862–8866.
31 P. Ramaswamy, N. E. Wong, B. S. Gelfand and G. K. H. Shimizu, Water stable magnesium MOF that conducts protons over 10^{-2} S cm^{-1}, *J. Am. Chem. Soc.*, 2015, **137**, 7640–7643.
32 A. D. G. Firmino, R. F. Mendes, M. M. Antunes, P. C. Barbosa, S. M. F. Vilela, A. A. Valente, F. M. L. Figueiredo, J. P. C. Tomé and F. A. Almeida Paz, Robust multifunctional yttrium-based metal–organic frameworks with breathing effect, *Inorg. Chem.*, 2017, **56**, 1193–1208.
33 P. Salcedo-Abraira, C. Biglione, S. M. Vilela, E. Svensson Grape, N. Ureña, F. Salles, M. T. Pérez-Prior, T. Willhammar, P. Trens, A. Várez, A. K. Inge and P. Horcajada, High proton conductivity of a bismuth phosphonate metal–organic framework with unusual topology, *Chem. Mater.*, 2023, **35**, 4329–4337.
34 *CrysAlisPRO, Version 1.0.43*, Oxford Diffraction/Agilent Technologies UK Ltd, Yarnton, U.K., 2020.
35 G. M. Sheldrick, Crystal structure refinement with SHELXL, *Acta Crystallogr., Sect. A*, 2015, **71**, 3–8.
36 G. M. Sheldrick, *SHELXT* –, integrated space-group and crystal-structure determination, *Acta Crystallogr., Sect. C*, 2015, **71**, 3–8.
37 O. V. Dolomanov, L. J. Bourhis, R. J. Gildea, J. A. K. Howard and H. Puschmann, OLEX2: a complete structure solution, refinement and analysis program, *J. Appl. Crystallogr.*, 2009, **42**, 339–341.
38 L. Palatinus and G. Chapuis, Superflip – a computer program for the solution of crystal structures by charge flipping in arbitrary dimensions, *J. Appl. Crystallogr.*, 2007, **40**, 786–790.
39 J. Rohlíček and M. Husák, MCE2005 – a new version of a program for fast interactive visualization of electron and similar density maps optimized for small molecules, *J. Appl. Crystallogr.*, 2007, **40**, 600–601.
40 V. Petříček, L. Palatinus, J. Plášil and M. Dušek, Jana2020 – a new version of the crystallographic computing system Jana, *Z. Kristallogr.*, 2023, **238**, 271–282.
41 *ZSimpWin, EChem Software, B. Yeum*, AMETEK Scientific Instruments, Ann Arbor (USA), 1999–2013.
42 E. Barsoukov and J. R. Macdonald, *Impedance Spectroscopy*, John Wiley & Sons Inc., New Jersey, 2018.
43 J. Jia, A. J. Blake, N. R. Champness, P. Hubberstey, C. Wilson and M. Schroder, Multi-dimensional transition-metal coordination polymers of 4,4′-bipyridine-N,N′-dioxide: 1D chains and 2D sheets, *Inorg. Chem.*, 2008, **47**, 8652–8664.
44 S. J. Lee, H. S. Kim, H. W. Yang, B. W. Yoo and C. M. Yoon, Synthesis of diethyl pyridin-2-ylphosphonates and quinolin-2-ylphosphonates by deoxygenative phosphorylation of the corresponding N-oxides, *Bull. Korean Chem. Soc.*, 2014, **35**, 2155–2158.
45 V. Penicaud, F. Odobel and B. Bujoli, Facile and efficient syntheses of 2,2′-bipyridine-based bis(phosphonic) acids, *Tetrahedron Lett.*, 1998, **39**, 3689–3692.
46 L. Sarkisov and A. Harrison, Computational structure characterisation tools in application to ordered and disordered porous materials, *Mol. Simul.*, 2011, **37**, 1248–1257.
47 T.-T. Wang, Y.-M. Su, C.-Q. Jiao, X.-O. Cai, H.-M. Sun, Y.-Y. Zhu and Z.-G. Sun, Lanthanide oxalatophosphonates with two types of layered structures: syntheses, structures, luminescence and magnetic properties, *New J. Chem.*, 2018, **42**, 1235–1242.
48 L. Wegner, D. M. Venturi, E. Ikonnikova, K. Hetze, J. Theissen, E. Derveaux, M. Oschatz, T. Willhammar and N. Stock, CAU-63, an Ultramicroporous Al-MOF with a Honeycomb-Shaped 2D IBU, *Inorg. Chem.*, 2025, **64**, 20254–20261.
49 F. Al-Ali, A. Lebugle, I. Rico-Lattes and G. Etemad-Moghadam, Preparation and characterization of new hybrid organic/inorganic systems derived from calcium (α-aminoalkyl)-phosphonates and -phosphonocarboxylates, *J. Colloid Interface Sci.*, 2005, **289**, 504–511.
50 D. Dollimore, J. Dollimore and P. D. Perry, The thermal decomposition of oxalates. Part VIII. Thermogravimetric and X-ray analysis study of the decomposition of aluminium oxalate, *J. Chem. Soc. A*, 1967, **1967**, 448–450.
51 A. Schmalz, C. G. Eby, C. Moss, B. Bhattachaya and F. Emmerling, Thermally Robust 1D Cu(I) Phosphonate Coordination Polymer Exhibiting Enhanced Proton Conductivity via Humidity-Driven Pathways, *Z. Anorg. Allg. Chem.*, 2026, **652**, e202500187.

52 C. Jia, S. Liang, Y.-X. Wen, Z.-Z. Xue, J.-X. Hu and G.-M. Wang, Photochromic Ln-Phosphonates Assembled by an Imidazole Derivative: Construction, Crystal Structures, and Light-Enhanced Proton Conductivity, *Cryst. Growth Des.*, 2024, **24**, 2202–2209.

53 R. M. P. Colodrero, G. K. Angeli, M. Bazaga-Garcia, P. Olivera-Pastor, D. Vilemin, E. R. Losilla, E. Q. Martos, G. B. Hix, M. A. G. Aranda, K. D. Demadis and A. Cabeza, Structural variability in multifunctional metal xylenediaminetetraphosphonate hybrids, *Inorg. Chem.*, 2013, **52**, 8770–8783.

54 S. Ondrušová, D. Bůžek, J. Hynek, T. Plecháček, L. Kubíčková, M. Veverka, T. Kmječ, M. Rozprým, J. Kohout and M. Kloda, Magnetism, Mössbauer spectroscopy, and proton conductivity of coordination polymers based on phosphonate and phosphinate linkers, *J. Phys. Chem. C*, 2025, **129**, 15850–15864.

55 Y. Shigeta, R. Asano, T. Kurihara, S. Amemori, T. Ida and M. Mizuno, Impact of acid–base amounts on proton conductivity and molecular dynamics of phosphonic acid-modified mesoporous silica/imidazole composites, *J. Phys. Chem. C*, 2025, **129**, 6032–6040.

56 M. Bazaga-García, R. M. P. Colodrero, M. Papadaki, P. Garczarek, J. Zoń, P. Olivera-Pastor, E. R. Losilla, L. León-Reina, M. A. G. Aranda, D. Choquesillo-Lazarte, K. D. Demadis and A. Cabeza, Guest Molecule-Responsive Functional Calcium Phosphonate Frameworks for Tuned Proton Conductivity, *J. Am. Chem. Soc.*, 2014, **136**, 5731–5739.

57 J. Wegener, A. Kaltbeitzel, R. Graf, M. Klapper and K. Müllen, Proton Conductivity in Doped Aluminum Phosphonate Sponges, *ChemSusChem*, 2014, **7**, 1148–1154.

58 (*a*) CCDC 2499442: Experimental Crystal Structure Determination, 2026, DOI: 10.5517/ccdc.csd.cc2pww5n; (*b*) CCDC 2499447: Experimental Crystal Structure Determination, 2026, DOI: 10.5517/ccdc.csd.cc2pwwbt; (*c*) CCDC 2499450: Experimental Crystal Structure Determination, 2026, DOI: 10.5517/ccdc.csd.cc2pwwfx; (*d*) CCDC 2503831: Experimental Crystal Structure Determination, 2026, DOI: 10.5517/ccdc.csd.cc2q1frz.